

Skyrmion soliton motion on periodic substrates by atomistic and particle based simulations

J. C. B. SOUZA¹, N. P. VIZARIM¹, C. J. O. REICHHARDT², C. REICHHARDT² and P. A. VENEGAS³

¹ POSMAT - Programa de Pós-Graduação em Ciência e Tecnologia de Materiais, São Paulo State University (UNESP), School of Sciences, Bauru 17033-360, SP, Brazil

² Theoretical Division and Center for Nonlinear Studies, Los Alamos National Laboratory, Los Alamos, New Mexico 87545, USA

³ Department of Physics, São Paulo State University (UNESP), School of Sciences, Bauru 17033-360, SP, Brazil

*** Missing PACS ***

Abstract – We compare the dynamical behavior of magnetic skyrmions interacting with square and triangular defect arrays just above commensuration using both an atomistic model and a particle-based model. Under an applied drive, the initial motion is a kink traveling through the pinned skyrmion lattice. For the square defect array, both models agree well and show a regime in which the soliton motion is locked along 45° . The atomistic model also produces locking of a soliton along 30° , while the particle-based model does not. For the triangular defect array, the atomistic model exhibits soliton motion locked to 30° over a wide region of external driving force values. In contrast, the particle-based model gives soliton motion locked to 45° over only a small range of external driving force values. The difference arises because the nondeforming particle model facilitates meandering skyrmion orbits while the deformable atomistic model enables stronger skyrmion-skyrmion interactions that reduce the meandering. Our results indicate that soliton motion through pinned skyrmion lattices on a periodic substrate is a robust effect and could open the possibility of using solitons as information carriers. Our results also provide a better understanding of the regimes for which particle-based models of skyrmions are best suited.

Introduction. – Solitons are nonlinear wave perturbations [1] that have been observed in a wide range of different science fields, including mathematics [2], chemistry [3,4], magnetism [5–11], and biology [12–14]. Due to their nonlinear spin dynamics, magnetic systems are particularly well able to stabilize magnetic solitons or nonlinear magnetic textures, which can take the form of magnetic vortices [9], magnon drops [10], magnetic skyrmions [15–17], hopfions [17–20], and bimerons [17, 21–23].

Solitons or kinks can also be stabilized in assemblies of particles coupled to a periodic substrate [24, 25]. When the number of particles equals the number of potential minima, the system should be free of kinks; however, if the number of particles is slightly higher or lower so that the system is off commensuration, localized kinks appear that depin under applied drive levels which can be much lower than the drive at which the bulk of the particles depin. Kink motion at incommensurate fillings on periodic substrates has been studied for colloidal particles [26–28], superconducting vortices [29,30] and various friction mod-

els [31,32]. Since skyrmions are also particle-like textures, when they are placed on a periodic substrate, kinks or solitons could also be stabilized in the skyrmion lattice. Recent work by Vizariim *et al.* [5] has shown the possibility of creating and moving a soliton along quasi one-dimensional chains of skyrmions using a particle based model. After this study, Souza *et al.* [6] demonstrated with an atomistic model that soliton motion along skyrmion chains is stable and that the soliton exhibited higher velocities than free skyrmions. The work on the quasi-one-dimensional systems opened the possibility of using soliton or kink motion in magnetic skyrmions as an information transfer method for new types of soliton-based devices employing skyrmions. An open question is whether soliton motion through skyrmion lattices remains stable in more realistic fully two-dimensional systems, whether the soliton behavior can be captured using both particle-based and atomistic models, and where the two models agree or disagree.

Magnetic skyrmions are particle-like topologically protected magnetic textures [15,33] that exhibit many simi-

larities to overdamped particles: they minimize their repulsive interactions by forming a triangular array, can be set in motion by the application of external drives, and can interact with material defects in a variety of ways [25, 34, 35]. The key difference between skyrmions and other overdamped particles is the presence of a non-dissipative Magnus force that causes skyrmions to move in the absence of disorder at an angle known as the intrinsic skyrmion Hall angle, $\theta_{\text{sk}}^{\text{int}}$, with respect to the external driving force [15, 16, 36–39]. In order to simulate all of the degrees of freedom of a skyrmion, it is necessary to use computationally expensive models, such as the atomistic model [40], that can capture behavior such as skyrmion annihilation, creation and deformation. To mitigate the computational expense of skyrmion simulations, Lin *et al.* [39] proposed a particle-based model for skyrmions that assumes the skyrmions remain rigid, an approximation that is valid for low skyrmion densities and low external currents.

Using atomistic simulations and particle based simulations, we study the dynamical behavior of soliton motion in magnetic skyrmion lattices on square and triangular substrates just away from commensuration that are subjected to an external driving force. For the square substrate, both models produce soliton motion along a 45° angle; however, the atomistic model exhibits an additional 30° soliton motion that is absent in the particle based model. At higher drives, the entire skyrmion lattice depins, and the transitions between the the different soliton and skyrmion flow phases are visible as changes in the transport curves and average Hall angle of the kink or skyrmion motion. For the triangular substrate, we also find regimes of stable soliton motion, but the models show substantial differences. The atomistic model exhibits soliton motion along a 30° angle for a wide range of external driving forces, whereas the particle model produces soliton motion along a 45° angle for a small range of external driving forces. In the particle model, the trajectory of the soliton is much more meandering, resulting in flow around an average angle of 45° , while in the atomistic model, the finite size of the skyrmions reduces the amount of meandering flow that occurs, causing motion along 30° to be more stable.

Methods. – We model Néel skyrmions in thin films with a magnetic field applied perpendicular to the film at zero temperature, $T = 0$ K, with periodic boundary conditions along the x and y directions. We use two distinct models, the atomistic model and the particle based model. Common substrate defect arrangements of N_m defects are used in both models. The square array of defects is modeled as $\phi_S(x, y) = \frac{A}{4} \left[\cos\left(\frac{2\pi x}{a_0}\right) + \cos\left(\frac{2\pi y}{a_0}\right) + 2 \right]$, where A is the defect strength and a_0 is the substrate lattice constant. The values of A and a_0 are different between each model and are listed below in the subsections describing the individual models. The triangular array of defects

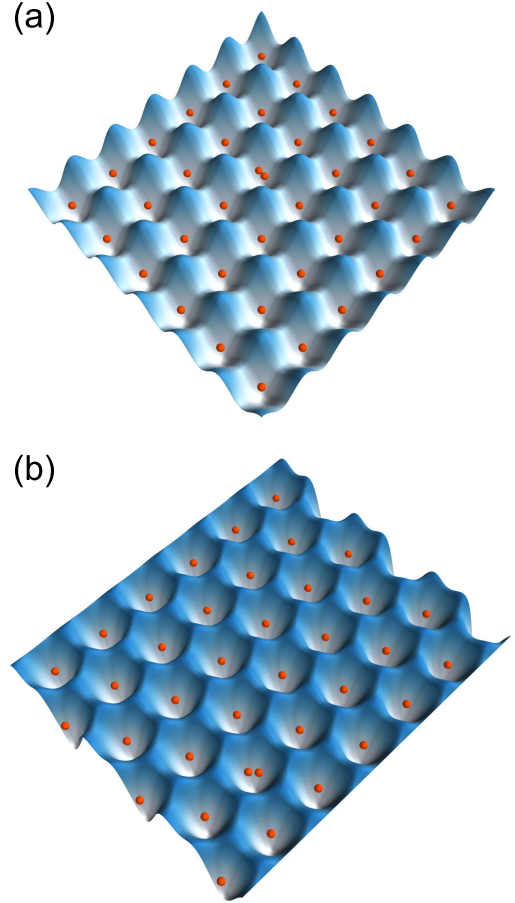


Fig. 1: A three-dimensional rendering of the system for (a) a square substrate potential and (b) a triangular substrate potential. Each minimum captures one skyrmion, and a single extra skyrmion has been placed inside the sample in order to create a kink or incommensuration.

is modeled as $\phi_T(x, y) = \sum_{i=1}^3 \frac{A}{2} \left[\cos\left(\frac{2\pi b_i}{a_0}\right) + 1 \right]$, with $b_i = x \cos(\theta_i) - y \sin(\theta_i) + a_0/2$ and $\theta_1 = \pi/6$, $\theta_2 = \pi/2$, $\theta_3 = 5\pi/6$. As in the square array, A is the defect strength and a_0 the substrate lattice constant, with different values of A and a_0 used for each model. For both models we choose values of a_0 such that there are $N_m = 36$ minima in the defect arrangement. We select the number of skyrmions N_{sk} to be just above commensuration with the substrate, $N_{\text{sk}} = N_m + 1 = 37$. In fig. 1(a,b), we show a three-dimensional rendering of the square and triangular defect arrays. Each potential minimum captures a single skyrmion, and we add one additional skyrmion to the sample in order to create a kink or soliton that can depin at a much lower drive than the commensurate skyrmions.

Atomistic Simulations. The atomistic model tracks the state of individual atomic magnetic moments [40]. The Hamiltonian describing the interactions of thin films at $T = 0$ K with an underlying square atomic arrangement

with lattice parameter $a = 0.5$ nm is given by [15, 37, 40]

$$\mathcal{H} = -\sum_{i,j \in N} J_{ij} \mathbf{m}_i \cdot \mathbf{m}_j - \sum_{i,j \in N} \mathbf{D}_{ij} \cdot (\mathbf{m}_i \times \mathbf{m}_j) - \sum_i \mu \mathbf{H} \cdot \mathbf{m}_i - \sum_i K(x_i, y_i) (\mathbf{m}_i \cdot \hat{\mathbf{z}})^2.$$

The first term on the right side is the exchange interaction between the nearest neighbors contained in the set N , with an exchange constant of $J_{ij} = J$ between magnetic moments i and j . The second term is the interfacial Dzyaloshinskii–Moriya interaction, where $\mathbf{D}_{ij} = D\hat{\mathbf{z}} \times \hat{\mathbf{r}}_{ij}$ is the Dzyaloshinskii–Moriya vector between magnetic moments i and j and $\hat{\mathbf{r}}_{ij}$ is the unit distance vector between sites i and j . The third term is the Zeeman interaction with an applied external magnetic field \mathbf{H} . Here $\mu = \hbar\gamma$ is the magnitude of the magnetic moment and $\gamma = 1.76 \times 10^{11} \text{T}^{-1} \text{s}^{-1}$ is the electron gyromagnetic ratio. The last term represents the perpendicular magnetic anisotropy (PMA) of the sample, where x_i and y_i are the spatial coordinates of the i magnetic moment. We use $K(x_i, y_i) = \phi_S(x_i, y_i)$ for a square array of defects and $K(x_i, y_i) = \phi_T(x_i, y_i)$ for a triangular array of defects. In ultrathin films, long-range dipolar interactions can be neglected [41].

The time evolution of the individual atomic magnetic moments is given by the LLG equation [42, 43]

$$\frac{\partial \mathbf{m}_i}{\partial t} = -\gamma \mathbf{m}_i \times \mathbf{H}_i^{\text{eff}} + \alpha \mathbf{m}_i \times \frac{\partial \mathbf{m}_i}{\partial t} + \frac{pa^3}{2e} (\mathbf{j} \cdot \nabla) \mathbf{m}_i. \quad (2)$$

Here $\mathbf{H}_i^{\text{eff}} = -\frac{1}{\hbar\gamma} \frac{\partial \mathcal{H}}{\partial \mathbf{m}_i}$ is the effective magnetic field including all interactions from the Hamiltonian, α is the Gilbert damping, and the last term is the spin-transfer-torque (STT), where p is the spin polarization, e is the electron charge, and $\mathbf{j} = j\hat{\mathbf{x}}$ is the applied current density. The STT current assumes that the conduction electron spins are always parallel to the magnetic moments \mathbf{m} [37, 44], and the driving force from the STT current [45] acts perpendicular to \mathbf{j} . We fix $\alpha = 0.3$, $J = 1$ meV, $D = 0.5J$, and $\mu\mathbf{H} = 0.6(D^2/J)(-\hat{\mathbf{z}})$. The resulting skyrmions move at an intrinsic skyrmion Hall angle of $\theta_{\text{sk}}^{\text{int}} = 64^\circ$ with respect to the driving force exerted by external currents. For both the square and triangular defect arrays we use $A = 0.1J$ and $a_0 = 14$ nm. The sample dimensions are $84 \text{ nm} \times 84 \text{ nm}$ for the square array of defects, and $(2/\sqrt{3})84 \text{ nm} \times 84 \text{ nm}$ for the triangular array of defects. The difference in sample size is required to properly apply boundary conditions.

Particle Based Simulations. The particle based simulations are governed by the equation of motion [39]

$$\alpha_d \mathbf{v}_i + \alpha_m \hat{\mathbf{z}} \times \mathbf{v}_i = \sum_{i \neq j} \mathbf{F}_{\text{sk}}(\mathbf{r}_{ij}) + \mathbf{F}_{\text{P}}(\mathbf{r}_i) + \hat{\mathbf{z}} \times \mathbf{F}_D, \quad (3)$$

where \mathbf{v}_i is the velocity of skyrmion i . The first term on the left side is the damping term, α_d , which can be written [37, 46] as $\alpha_d = -\alpha \mathcal{D}$, where α is the Gilbert damping and

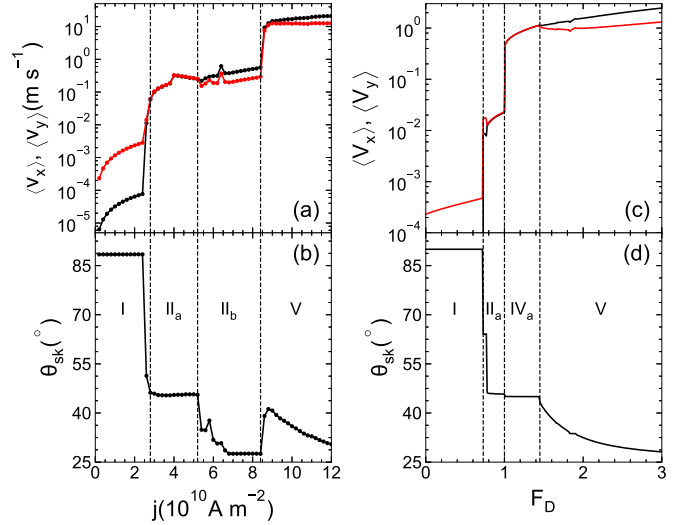


Fig. 2: Velocity curves and the corresponding skyrmion Hall angle θ_{sk} obtained from (a, b) atomistic simulations and (c, d) particle based simulations for the square defect array. (a) $\langle v_x \rangle$ (black) and $\langle v_y \rangle$ (red) vs applied current j . (b) The corresponding θ_{sk} vs j . (c) $\langle v_x \rangle$ (black) and $\langle v_y \rangle$ (red) vs driving force F_D . (d) The corresponding θ_{sk} vs F_D . Dashed lines delimit the different phases. I: pinned state. II_a: soliton motion along 45° . II_b: soliton motion along 30° . IV_a: all skyrmions moving along 45° . V: all skyrmions moving with no locking angle.

\mathcal{D} is the dissipative tensor. The second term is the Magnus force where the Magnus strength α_m can be written [37, 46] as $\alpha_m = -4\pi Q$, where Q is the skyrmion charge. The ratio α_m/α_d determines the intrinsic skyrmion Hall angle $\theta_{\text{sk}}^{\text{int}} = \arctan(\alpha_m/\alpha_d)$. In order to match the particle based θ_{sk} to the atomistic θ_{sk} , we use values of α_m and α_d such that $\theta_{\text{sk}}^{\text{int}} = \arctan(\alpha_m/\alpha_d) = 64^\circ$. The first term on the right side of eq. 3 is the skyrmion-skyrmion interaction given by $\mathbf{F}_{\text{sk}}(\mathbf{r}_{ij}) = -U_{\text{sk}}K_1(r_{ij})\hat{\mathbf{r}}_{ij}$, where $U_{\text{sk}} = 1$ is the interaction strength and K_1 is the modified first order Bessel function. The second term is the interaction with the underlying substrate potential, given by $\mathbf{F}_{\text{P}}(\mathbf{r}_i) = -\nabla\phi_S(\mathbf{r}_i)$ for the square array of defects and $\mathbf{F}_{\text{P}}(\mathbf{r}_i) = -\nabla\phi_T(\mathbf{r}_i)$ for the triangular array of defects. In both defect arrays, the potential strength is $A = 4$ and the substrate lattice constant is $a_0 = 6$. The last term is the interaction with an external drive, $\mathbf{F}_D = F_D\hat{\mathbf{x}}$, which is in accordance with the action of an STT current on magnetic skyrmions [37, 45, 46]. Our simulation box is of size 36×36 for the square defect array and $(2/\sqrt{3})36 \times 36$ for the triangular defect array.

Square array. – We first compare the dynamics of skyrmions interacting with a square array of defects in atomistic and particle-based simulations. In fig. 2(a), we plot $\langle v_x \rangle$ and $\langle v_y \rangle$ versus applied current j , and in fig. 2(b), we show the corresponding effective $\theta_{\text{sk}} = \arctan(\langle v_y \rangle / \langle v_x \rangle)$ versus j from the atomistic simulation. We observe four dynamical phases: a pinned phase I with

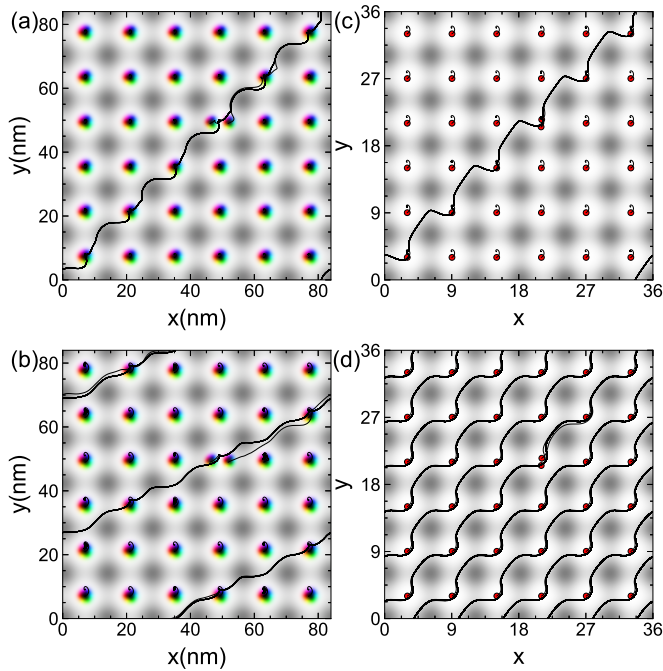


Fig. 3: Skymion trajectories (black lines) and the location of substrate minima (white) and maxima (gray) in the square defect array for (a, b) atomistic simulations where the skyrmions appear as colored disks and (c, d) particle based simulations where the skyrmions are drawn as red disks. (a) Atomistic simulation at $j = 4 \times 10^{10} \text{ A m}^{-2}$, corresponding to phase II_a from fig. 2(a, b). (b) Atomistic simulation at $j = 8 \times 10^{10} \text{ A m}^{-2}$, corresponding to phase II_b from fig. 2(a, b). (c) Particle based simulation at $F_D = 0.8$, corresponding to phase II_a in fig. 2(c, d). (d) Particle based simulation at $F_D = 1.2$, corresponding to phase IV_a in fig. 2(c, d). Animations showing the motion of the skyrmions are available in the Supplemental Material [47].

no skyrmion motion, phase II_a where a soliton moves along 45° , phase II_b in which a soliton moves at 30° , and phase V in which all of the skyrmions depin and move without locking to any direction. The skyrmion motion in phases II_a and II_b is illustrated in fig. 3(a, b).

Figure 2(c, d) shows $\langle v_x \rangle$, $\langle v_y \rangle$, and θ_{sk} versus F_D from particle based simulations of skyrmions interacting with a square array of defects. We again observe four dynamical phases, which are a pinned phase I, phase II_a with soliton motion along 45° , phase IV_a in which all of the skyrmions depin and move along $\theta_{\text{sk}} = 45^\circ$, and phase V where all of the skyrmions have depinned but move without locking to any direction. The skyrmion motion in phases II_a and IV_a is illustrated in fig. 3(c, d).

Figure 3(a) shows the skyrmion trajectories during the phase II_a soliton motion along 45° from the atomistic model. Here, the extra skyrmion shares an anisotropy minimum with another skyrmion, and the skyrmion-skyrmion interaction force between the two lowers the depinning force at which one of the skyrmions can escape from the minimum and become an interstitial skyrmion. The interstitial skyrmion moves across the anisotropy

landscape until it reaches another anisotropy minimum containing a pinned skyrmion. Through skyrmion-skyrmion interactions, the interstitial skyrmion pushes the pinned skyrmion out of the anisotropy minimum and takes up residence in the minimum. The displaced skyrmion becomes the new interstitial skyrmion, and this pattern of motion repeats indefinitely. In fig. 3(b) we illustrate the skyrmion trajectories during the phase II_b soliton motion along 30° using the atomistic model. The mechanism of motion is identical to that observed in fig. 3(a), but now the interstitial skyrmion encounters a pinned skyrmion along the 30° angle line instead of the 45° angle line.

Figure 3(c) shows the skyrmion trajectories during the phase II_a soliton motion at 45° obtained from the particle based model. The behavior is identical to that found in the atomistic model, where the skyrmion-skyrmion interactions cause the extra skyrmion trapped inside a potential minimum to depin at low F_D . Since the skyrmion is treated as a point particle, the trajectory differs in detail from the atomistic trajectory shown in fig. 3(a); however, the mechanism of exchange between interstitial and pinned skyrmions remains the same. In fig. 3(d) we show the skyrmion trajectories in phase IV_a from the particle based model where all of the skyrmions have depinned and move along 45° . Here the extra skyrmion does not play a major role, since all of the skyrmions are interacting with the potential in an ordered manner and following a 45° trajectory. The skyrmion lattice is similar to a moving crystal but contains a localized defect produced by the extra skyrmion.

We note that previous work on skyrmions moving over a two-dimensional square periodic substrate under an increasing drive showed a directional locking effect in which the skyrmion motion locked to particular symmetry angles of the substrate [48,49]. Continuum models for individual skyrmions on antidot lattices also produce similar directional locking [45,50]. The results we describe here are different in that the motion is not of individual continuously moving skyrmions but of kink traveling through a skyrmion lattice, so the locking is a collective effect instead of a single particle effect. Additionally, the applied drive needed to produce kink motion is substantially lower than the drive at which an isolated skyrmion would depin from the substrate potential minimum. The reduction in the driving threshold would be particularly useful for applications.

Triangular array. – We next compare the dynamical behavior of skyrmions on a triangular defect array in atomistic simulations and particle based simulations. For the atomistic simulations, fig. 4(a) shows $\langle v_x \rangle$ and $\langle v_y \rangle$ versus j , while in fig. 4(b) we plot the corresponding θ_{sk} versus j . We observe three dynamical phases. At low drives, we find a pinned phase I. There is a transitional phase III_a of disordered soliton motion, where soliton transport occurs but does not follow a well defined direction. At higher drives, phase II_b appears in which

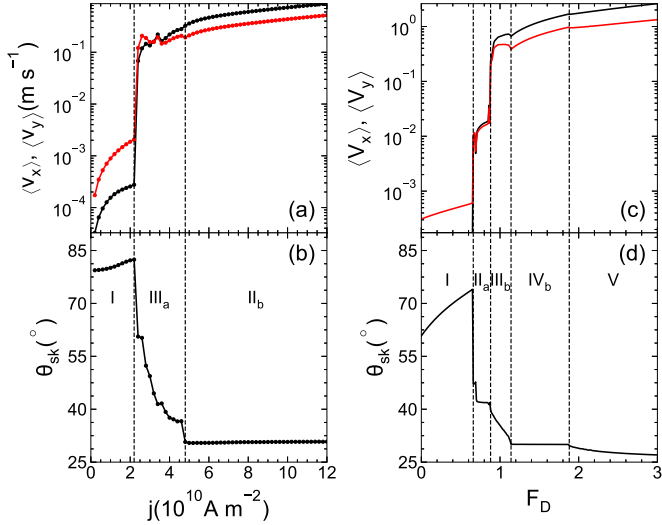


Fig. 4: Velocity curves and the corresponding skyrmion Hall angle θ_{sk} obtained from (a, b) atomistic simulations and (c, d) particle based simulations for the triangular defect array. (a) $\langle v_x \rangle$ (black) and $\langle v_y \rangle$ (red) vs applied current j . (b) The corresponding θ_{sk} vs j . (c) $\langle V_x \rangle$ (black) and $\langle V_y \rangle$ (red) vs driving force F_D . (d) The corresponding θ_{sk} vs F_D . Dashed lines delimit different phases: I: pinned state. II_a: soliton motion along 45° . II_b: soliton motion along 30° . III_a: disordered soliton motion. III_b: completely disordered flow. IV_b: all skyrmions moving along 30° . V: all skyrmions moving without locking to any direction.

the soliton moves along 30° . Over the range of j values that we consider, we never observe a completely depinned state, but we expect that for larger values of j , the pinned skyrmions would eventually escape from the anisotropy minima and move throughout the sample. The skyrmion trajectories in phases III_a and II_b are illustrated in fig. 5(a, b).

In fig. 4(c), we plot $\langle V_x \rangle$ and $\langle V_y \rangle$ versus F_D for a particle based simulation of skyrmions driven over a triangular defect array, and in fig. 4(d) we show the corresponding θ_{sk} versus F_D . Five dynamical phases appear. At low drives, we find a pinned phase I. Phase II_a is soliton motion along 45° , and it is followed by a transitional phase III_b in which a small number of skyrmions are present simultaneously and move chaotically across the system. In phase IV_b, all of the skyrmions are moving along 30° , and phase V consists of all of the skyrmions moving without locking to any direction. Illustrations of the skyrmion trajectories for phases II_a and IV_b appear in fig. 5(c, d).

Unlike what we found for the square defect array, here the atomistic model and the particle based model do not exhibit good agreement. A pinned phase is present in both cases, but as we increase the drive, in the atomistic simulations we observe a wide phase II_b 30° soliton motion over the range $4.8 \times 10^{10} \text{ A m}^{-2} \leq j \leq 12 \times 10^{10} \text{ A m}^{-2}$. In comparison, for the particle based simulations there is a small window of phase II_a 45° soliton motion over the

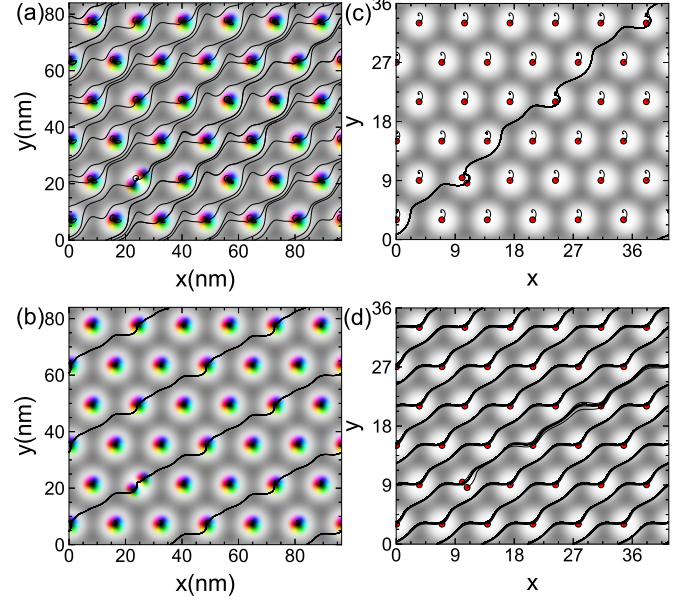


Fig. 5: Skyrmion trajectories (black lines) and the location of substrate minima (white) and maxima (gray) in the triangular defect array for (a, b) atomistic simulations where the skyrmions appear as colored disks and (c, d) particle based simulations where the skyrmions are drawn as red disks. (a) Atomistic simulation at $j = 4 \times 10^{10} \text{ A m}^{-2}$, corresponding to phase III_a in fig. 4(a, b). (b) Atomistic simulation at $j = 8 \times 10^{10} \text{ A m}^{-2}$, corresponding to phase II_b in fig. 4(a, b). (c) Particle based simulation at $F_D = 0.8$, corresponding to phase II_a in fig. 4(c, d). (d) Particle based simulation at $F_D = 1.5$, corresponding to phase IV_b in fig. 4(c, d). Animations showing the skyrmion motion are available in the Supplemental Material [47].

range $0.66 \leq F_D \leq 0.88$. The phase II_b 30° angle soliton motion is absent in the particle based simulations. This large difference in behavior is likely due to the fact that in the atomistic simulations, the skyrmion has a finite size and is able to deform, as is visible by comparing the phase II_a flow in fig. 3(a) to that in fig. 3(c), or comparing the phase II_b flow in fig. 5(b) to the phase II_a flow in fig. 5(c). For higher values of F_D , the behavior of the atomistic and particle based simulations diverge significantly. The particle based simulation produces phase IV_b flow in which all of the skyrmions move along 30° , followed by phase V flow in which all of the skyrmions move without locking to a particular direction, while the atomistic simulations remain trapped in phase II_b with soliton motion along 30° .

Figure 5(a) shows the trajectories of skyrmions interacting with a triangular defect array from atomistic simulations performed at $j = 4 \times 10^{10} \text{ A m}^{-2}$, corresponding to phase III_a in fig. 4(a, b). The soliton mechanism of motion described previously still occurs here, but the soliton does not lock to any angle and gradually works its way all around the sample. When we increase the external current to $j = 8 \times 10^{10} \text{ A m}^{-2}$, corresponding to phase II_b in fig. 4(a, b), the skyrmions move as illustrated in

fig. 5(b). Again, we observe a soliton motion, but unlike what was shown in fig. 5(a), the motion occurs along a well defined angle of 30° . This motion appears over the range $4.8 \times 10^{10} \text{A m}^{-2} \leq j \leq 12 \times 10^{10} \text{A m}^{-2}$.

In fig. 5(c) we illustrate the skyrmion trajectories for motion over a triangular defect array from particle based simulations with $F_D = 0.8$, corresponding to the phase II_a flow in fig. 4(c, d). For this value of F_D , a soliton moves across the sample at 45° . We observe the 45° soliton motion only in the particle based simulations and do not find it in the atomic simulations. When we increase F_D to $F_D = 1.5$, corresponding to phase IV_b in fig. 4(c, d), all of the skyrmions flow along 30° , as shown in fig. 5(d). Similar to what we found in fig. 3(d), the skyrmion lattice travels as a moving crystal that contains a localized defect produced by the extra skyrmion.

The difference in the angle of soliton motion on a triangular defect array between the atomistic and particle based models can be explained by the finite skyrmion size in the atomistic simulations. The barrier between anisotropy minima is enhanced when the skyrmion has a finite size, whereas in the particle based simulations, the pointlike nature of the skyrmions gives a reduced barrier between anisotropy minima. The larger barrier potential created by the finite skyrmion size can be observed by comparing the trajectory of an interstitial skyrmion as it passes between two anisotropy minima; the trajectories in the atomistic simulation exhibit fewer meanders compared to the trajectories in the particle based simulations. The increase in the barrier potential forces the atomistic interstitial skyrmion to move following the 30° angle imposed by the triangular lattice, whereas the interstitial skyrmion in the particle based model can travel along a wider range of paths between substrate minima. To compensate for the overly unconstrained mobility of skyrmions the particle based model, the barrier between potential minima can be increased either by increasing the skyrmion-skyrmion interaction strength U_{sk} or reducing the lattice constant of the substrate potential. In principle, it may be possible to identify simulation parameters for the particle model of the triangular substrate that would match the behavior of the atomistic simulations and compensate for the rigidity and vanishing size of the particle-based skyrmion model.

Summary. – We compared the results of atomistic simulations and particle based simulations of soliton motion for skyrmion assemblies just past commensuration on both square and triangular substrates. For the square array, both models agree well at low and high drives, but differ for intermediate drives. The atomistic model produces a pinned phase, soliton motion along 45° , soliton motion along 30° , and unlocked flow of all skyrmions. The soliton motion proceeds via the replacement by an interstitial skyrmion of a pinned skyrmion in an anisotropy minimum, with the depinned skyrmion becoming the new interstitial skyrmion. The particle based model produces a pinned phase, soliton motion along 45° , a phase where

all of the skyrmions move along 45° , and unlocked flow of all skyrmions. The particle based model does not exhibit the 30° soliton motion found in the atomistic simulations, and the trajectories in the particle based model meander more than the atomistic model trajectories due to the rigidity and vanishing size of the particle based skyrmions. For both models, the different dynamic phases are visible as signatures in the velocity-force curves, skyrmion Hall angle, and skyrmion trajectories.

The atomistic and particle based models do not agree well on the motion of skyrmions over a triangular defect array. The atomistic model produces a pinned phase, a transitional phase in which a soliton moves with no well defined angle, and a regime of soliton motion at 30° that spans a wide range of external drive values. The particle based model exhibits a pinned phase, soliton motion along 45° , a transitional phase in which all skyrmions participate in disordered soliton motion, a phase in which all of the skyrmions move along 30° , and unlocked motion of all of the skyrmions. Here only the pinned phase is common between the two models.

Our results provide a better understanding of the regimes in which the particle model is a good or a poor approximation for the skyrmion motion. We argue that it can be possible to mitigate the approximations made in the particle based model by adjusting the strength of the interactions between the skyrmions or modifying the lattice constant of the substrate. Our results will be beneficial for determining how to control skyrmion soliton motion using a combination of anisotropy trapping and external driving.

* * *

We gratefully acknowledge the support of the U.S. Department of Energy through the LANL/LDRD program for this work. This work was supported by the US Department of Energy through the Los Alamos National Laboratory. Los Alamos National Laboratory is operated by Triad National Security, LLC, for the National Nuclear Security Administration of the U. S. Department of Energy (Contract No. 892333218NCA000001). J.C.B.S acknowledges funding from Fundação de Amparo à Pesquisa do Estado de São Paulo - FAPESP (Grant 2023/17545-1). We would like to thank Dr. Felipe F. Fanchini for providing the computational resources used in this work. These resources were funded by the Fundação de Amparo à Pesquisa do Estado de São Paulo - FAPESP (Grant: 2021/04655-8).

REFERENCES

[1] SCOTT A. C., CHU F. Y. F. and McLAUGHLIN D. W., *Proceedings of the IEEE*, **61** (1973) 1443.
 [2] MANUKURE S. and BOOKER T., *Partial Diff. Eq. Appl. Math.*, **4** (2021) 100140.

- [3] HEEGER A. J., KIVELSON S., SCHRIEFFER J. R. and SU W. P., *Rev. Mod. Phys.*, **60** (1988) 781.
- [4] TOLBERT L. M., *Accounts Chem. Res.*, **25** (1992) 561.
- [5] VIZARIM N. P., SOUZA J. C. B., REICHHARDT C. J. O., REICHHARDT C., MILOŠEVIĆ M. V. and VENEGAS P. A., *Phys. Rev. B*, **105** (2022) 224409.
- [6] SOUZA J. C. B., VIZARIM N. P., REICHHARDT C. J. O., REICHHARDT C. and VENEGAS P. A., *J. Mag. Mag. Mater.*, **587** (2023) 171280.
- [7] GALKINA E. G. and IVANOV B. A., *Low Temp. Phys.*, **44** (2018) 618.
- [8] SLONCZEWSKI J. C., *AIP Conf. Proc.*, **5** (1972) 170.
- [9] PAPANICOLAOU N. and TOMARAS T. N., *Nucl. Phys. B*, **360** (1991) 425.
- [10] KOSEVICH A. M., IVANOV B. A. and KOVALEV A. S., *J. Phys. Colloq.*, **39** (1978) C6.
- [11] MÜHLBAUER S., BINZ B., JONIEZ F., PFLEIDERER C., ROSCH A., NEUBAUER A., GEORGII R. and BÖNI P., *Science*, **323** (2009) 915.
- [12] CIBLIS P. and COSIC I., *J. Theor. Biol.*, **184** (1997) 331.
- [13] ZHOU G.-P., *Phys. Scripta*, **40** (1989) 698.
- [14] DAVYDOV A. S., *J. Theor. Biol.*, **38** (1973) 559.
- [15] NAGAOSA N. and TOKURA Y., *Nature Nanotechnol.*, **8** (2013) 899.
- [16] JIANG W., ZHANG X., YU G., ZHANG W., WANG X., JUNGFLEISCH M. B., PEARSON J. E., CHENG X., HEINONEN O., WANG K. L., ZHOU Y., HOFFMANN A. and TE VELTHUIS S. G. E., *Nature Phys.*, **13** (2017) 162.
- [17] GÖBEL B., MERTIG I. and TRETIAKOV O. A., *Phys. Rep.*, **895** (2021) 1.
- [18] TAI J.-S. B. and SMALYUKH I. I., *Phys. Rev. Lett.*, **121** (2018) 187201.
- [19] LIU Y., LAKE R. K. and ZANG J., *Phys. Rev. B*, **98** (2018) 174437.
- [20] SUTCLIFFE P., *J. Phys. A: Math. Theor.*, **51** (2018) 375401.
- [21] NAGASE T., SO Y.-G., YASUI H., ISHIDA T., YOSHIDA H. K., TANAKA Y., SAITOH K., IKARASHI N., KAWAGUCHI Y., KUWAHARA M. and NAGAO M., *Nature Commun.*, **12** (2021) 3490.
- [22] OHARA K., ZHANG X., CHEN Y., KATO S., XIA J., EZAWA M., TRETIAKOV O. A., HOU Z., ZHOU Y., ZHAO G., YANG J. and LIU X., *Nano Lett.*, **22** (2022) 8559.
- [23] GÖBEL B., MOOK A., HENK J., MERTIG I. and TRETIAKOV O. A., *Phys. Rev. B*, **99** (2019) 060407.
- [24] BAK P., *Rep. Prog. Phys.*, **45** (1982) 587.
- [25] REICHHARDT C. and REICHHARDT C. J. O., *Rep. Prog. Phys.*, **80** (2017) 026501.
- [26] BOHLEIN T. and BECHINGER C., *Phys. Rev. Lett.*, **109** (2012) 58301.
- [27] VANOSSI A. and TOSATTI E., *Nature Mater.*, **11** (2012) 97.
- [28] MCDERMOTT D., AMELANG J., REICHHARDT C. J. O. and REICHHARDT C., *Phys. Rev. E*, **88** (2013) 062301.
- [29] REICHHARDT C., OLSON C. J. and NORI F., *Phys. Rev. Lett.*, **78** (1997) 2648.
- [30] GUTIERREZ J., SILHANEK A. V., VAN DE VONDEL J., GILLJNS W. and MOSHCHALOV V. V., *Phys. Rev. B*, **80** (2009) 140514.
- [31] BRAUN O. M., DAUXOIS T., PALIY M. V. and PEYRARD M., *Phys. Rev. Lett.*, **78** (1997) 1295.
- [32] VANOSSI A., MANINI N., URBAKH M., ZAPPERI S. and TOSATTI E., *Rev. Mod. Phys.*, **85** (2013) 529.
- [33] JE S.-G., HAN H.-S., KIM S. K., MONTOYA S. A., CHAO W., HONG I.-S., FULLERTON E. E., LEE K.-S., LEE K.-J., IM M.-Y. and HONG J.-I., *ACS Nano*, **14** (2020) 3251.
- [34] OLSON REICHHARDT C. J., LIN S. Z., RAY D. and REICHHARDT C., *Physica C*, **503** (2014) 52.
- [35] REICHHARDT C., REICHHARDT C. J. O. and MILOŠEVIĆ M., *Rev. Mod. Phys.*, **94** (2022) 035005.
- [36] LITZIUS K., LEMESH I., KRÜGER B., BASSIRIAN P., CARETTA L., RICHTER K., BÜTTNER F., SATO K., TRETIAKOV O. A., FÖRSTER J., REEVE R. M., WEIGAND M., BYKOVA I., STOLL H., SCHÜTZ G., BEACH G. S. D. and KLÄUI M., *Nature Phys.*, **13** (2017) 170.
- [37] IWASAKI J., MOCHIZUKI M. and NAGAOSA N., *Nature Commun.*, **4** (2013) 1463.
- [38] LIN S.-Z., REICHHARDT C., BATISTA C. D. and SAXENA A., *Phys. Rev. Lett.*, **110** (2013) 207202.
- [39] LIN S.-Z., REICHHARDT C., BATISTA C. D. and SAXENA A., *Phys. Rev. B*, **87** (2013) 214419.
- [40] EVANS R. F. L., *Atomistic Spin Dynamics in Handbook of Materials Modeling: Applications: Current and Emerging Materials*, edited by ANDREONI W. and YIP S., (Springer International Publishing) 2018 pp. 1–23.
- [41] PAUL S., HALDAR S., VON MALOTTKI S. and HEINZE S., *Nature Commun.*, **11** (2020) 4756.
- [42] SEKI S. and MOCHIZUKI M., *Skyrmions in Magnetic Materials* (Springer International Publishing) 2016.
- [43] GILBERT T. L., *IEEE Trans. Mag.*, **40** (2004) 3443.
- [44] ZANG J., MOSTOVOY M., HAN J. H. and NAGAOSA N., *Phys. Rev. Lett.*, **107** (2011) 136804.
- [45] FEILHAUER J., SAHA S., TOBIK J., ZELENT M., HEYDERMAN L. J. and MRUCZKIEWICZ M., *Phys. Rev. B*, **102** (2020) 184425.
- [46] EVERSCHOR-SITTE K., MASELL J., REEVE R. M. and KLÄUI M., *J. Appl. Phys.*, **124** (2018) 240901.
- [47] FOR SUPPLEMENTARY VIDEOS. S. S. M.,
- [48] REICHHARDT C., RAY D. and REICHHARDT C. J. O., *Phys. Rev. B*, **91** (2015) 104426.
- [49] REICHHARDT C. and REICHHARDT C. J. O., *Phys. Rev. B*, **105** (2022) 214437.
- [50] SUN W., WANG W., YANG C., LI X., LI H., HUANG S. and CHENG Z., *Phys. Rev. B*, **107** (2023) 184439.